NATIONAL UNIVERSITY OF SCIENCE AND TECHNOLOGY POLITEHNICA OF BUCHAREST (UNSTPB)

Doctoral School of Electronics, Telecommunications and Information Technology

Decision No. 120 from 26.10.2023

Ph.D. THESIS SUMMARY

Muhammad Amjad IQBAL

RECONSTRUCTIA IMAGINILOR SAR DE INALTA REZOLUTIE

SPARSE RECONSTRUCTION FOR HIGH-RESOLUTION INVERSE SAR IMAGING

THESIS COMMITTEE

Prof. dr. ing. Gheorghe BREZEANU UNSTPB	President
Prof. dr. ing. Andrei ANGHEL UNSTPB	PhD Supervisor
Prof. dr. ing. Emanuel PUSCHITA Technical University of Cluj-Napoca	Referee
Dr. ing. habil. Miguel HEREDIA CONDE University of Siegen, Germany	Referee
Dr. ing. Andreas BATHELT Fraunhofer Institute (FHR), Germany	Referee
Prof. dr. ing. Mihai DATCU UNSTPB	Referee

BUCHAREST 2023

Table of contents

Chapter 1

Introduction

Radar systems perform well in sensing during any weather condition, either rainy or cloudy, light, or dark times; hence, they act as primary sensors. In remote sensing, synthetic aperture radar (SAR) and Inverse SAR are vital for Earth observations and target detection. Motion, which results from the movement of the platform or target, is the key to radar imaging [1, 2].

1.1 The field of the doctoral thesis

ISAR provides images of objects that are rotated with respect to the radar. An efficient image-focusing algorithm is required to generate ISAR images from the echoes of the raw data. With the advancement of radar technology, imaging has become an important function of radars. The field of doctoral thesis is utilizing monostatic SAR data from Sentinel-1 for ocean remote sensing and Inverse SAR imaging by exploiting mmw-wave and X-band radars. Polarimetric data obtained from radar provides an opportunity to extract features, delineate targets, and reconstruct images using suitable polarization under given circumstances. Moreover, the decomposition of polarization enhances the extraction of properties and the required information. Radar data for sparse reconstruction is an emerging topic in compressive sensing for ISAR imaging. To reconstruct image of the target directly from raw data with a limited number of samples reduces the overhead of radar systems and improves the capabilities of radars to sense targets with short coherent processing intervals [3].

1.2 Scope of the doctoral thesis

The signal and image processing of SAR and ISAR data is the focus of this thesis. Several issues are addressed, including estimation of ocean circulation parameters based on Doppler centroid, SAR data preservation via complex-valued (CV) networks, coastline and ice-line delineation via constant false alarm rate (CFAR) methods, corporate or non-

corporate target detection via imaging, and compressive sensing for high resolution ISAR imaging. Future work is to adapt the newly developed parallel computing for along-track interferometry to advance the bistatic SAR systems for ocean current estimation. Also, high-resolution imaging of the required targets in unconstrained motion with fewer data samples will reduce the scanning time of SAR and ISAR systems.

1.3 The original content of the doctoral thesis

The particularly distinctive work presented in this thesis is categorized into three sections.

(i) The first part is a study on the Doppler centroid (f_{DC}) estimation for ocean surface current (OSC) retrieval using both Strip-map and TOPS SAR data [4]. Parallel computing advancement give is opportunity to reduce memory constraints for wide ocean area Doppler estimates. We developed de-ramping of TOPS data similar to the SOA methods which is user friendly and easy to adapt [5]. Also, we preserve Doppler properties of SAR data using novel CV architecture. Experimental and analytical results prove the practicality of the modified and proposed methodology for ocean remote sensing.

(ii) The second part is a study of SAR target detection by using CFAR detection algorithm. A novel method for coastline extraction based on Doppler centroid is proposed with concept of static coastline paves zero Doppler [6]. Furthermore, Subaperture (SA) decomposition method is used to generate multiple SA, which are then averaged to enhance TCR, whereas dual-pol correlation matrix is proposed for ship detection using CFAR approach. Extending this strategy to ice-cover extraction provided great results in multi-layer ice-cover extraction using CFAR. The method is experimentally and quantitatively evaluated for overall agreement between target and non-target detection.

(iii) The third and last section of the study covered compressive sensing, sparse feature extraction, and ISAR imaging for target detection. With the use of improved ISAR wave-number ($\omega - \mathrm{k}$) imaging, images can be focused with adequate resolution and with minimal computing expense. Then, by utilizing ISAR images and dual-pol $\mathrm{H} - \alpha$ decomposition, sparse characteristics of tree targets are retrieved. Finally, we were able to reconstruct ISAR images using only a limited amount of data samples thanks to coarse-to-fine (CTF) estimates, which took us very close to real-time target imaging.

Chapter 2

Doppler Centroid Estimation for OSC Retrieval

Accurate estimation of the f_{DC} of the received data is crucial in SAR processing. Poor estimates introduce noise and ambiguity levels in the processed image, often leading to a significant impact on image clarity. Precise estimation of the f_{DC} is challenging because measurements rely solely on geometry, and the received data may contain local anomalies that hinder the estimation process. An improper f_{DC} estimation can result in SNR loss, increased azimuth ambiguity, and the loss of specific information, such as surface current and wind speed.

2.1 Doppler Centroid Estimation

The main focus in this chapter is the use of a 2D convolution filter for the estimation of f_{DC} based the prevailing algorithms including CDE, SDE, and EB. The relative movement of the radar or the dynamic scene under observation exhibits Doppler shift, given as:

$$f_D = -\frac{k_{Rad} V}{\pi} \tag{2.1}$$

where k_{Rad} is the radar wave-number, and v is the line-of-sight velocity of the target. The Doppler centroid f_{DC} can be estimated from the SAR processed data. If the area under observation is stationary, the anormal Doppler shift will be zero. The prevailing algorithms to estimate f_{DC} either by finding the centroid of power spectrum of signal in the azimuth direction [7]; or through the phase of auto correlation function [8]; or correlation of real and imaginary parts of complex SAR data via sign alone.

2.1.1 Correlation Doppler Estimation (CDE)

The CDE method involves an cross-correlation of the SLC image 'S' with its shifted version 'S^*' in the azimuth direction '$\Delta\eta$'. [4]. By using the sliding window 'W' of

size $N \times N$ locally computed the correlation in the azimuth direction and performed an averaging operation in the range direction, The phase 'ϕ' of correlation term $C(\eta,\tau) = S \cdot S^*$ is estimated as:

$$\phi(\eta,\tau) = \arg\{\langle S(\eta,\tau)S^*(\Delta\eta,\tau)\rangle\} \tag{2.2}$$

Based on the pulse repetition frequency (PRF) and phase correlation function, the f_{DC} is calculated as follows:

$$f_{\mathrm{DC}}(\eta,\tau) = -\frac{\mathrm{PRF}}{2\pi}\phi(\eta,\tau) \tag{2.3}$$

2.1.2 Sign Doppler Estimation (SDE)

The Sign Doppler Estimation technique utilizes the correlation. The underlying principle of this approach revolves around harnessing the "arcsine law" inherent in a Gaussian process.

$$Y = \sin\left(\frac{\pi}{2}\, R\,[II, IQ, QI, QQ]\right) \tag{2.4}$$

where R contains correlation of each real (I) and imaginary (Q) parts, the sign function of signal $Z(t)$ is given as:

$$Z(t) = \begin{cases} 1, & for \quad Y(t) \geq 0 \\ -1, & for \quad Y(t) < 0 \end{cases} \tag{2.5}$$

since $Z(t)$ only takes value of +1 and -1 hence it is called sign of $Y(t)$. To estimate the Doppler, first obtain 4-sign correlations including $II, IQ, QI,$ and, QQ, then derive corresponding correlation coefficients and complex correlation coefficients, given as:

$$R(k) = \frac{1}{2}(\rho_{II} + \rho_{QQ}) + j\frac{1}{2}(\rho_{IQ} - \rho_{QI}) \tag{2.6}$$

finally convert argument of $R(k)$ to f_{DC} as given below:

$$f_{\mathrm{DC}}^{SDE} = \frac{\mathrm{PRF}}{2\pi\Delta\delta} \times (\arg\{R(k)\}) \tag{2.7}$$

2.1.3 Energy Balancing (EB)

Step-1 To estimate the f_{DC} by using energy balancing method, at first, calculate average power spectrum $S(n)$ in the azimuth direction.

Step-2 To achieve the reference function $R(f)$ and ensure EB is attained, the circular

cumulative summation is applied, so that the energy of spectrum equals on both sides:

$$R(f) = \begin{cases} -1, & \text{for } 0 \leq f \leq \frac{\text{PRF}}{2}, \\ +1, & \text{for } -\frac{\text{PRF}}{2} \leq f \leq 0, \\ 0, & \text{otherwise.} \end{cases} \tag{2.8}$$

Step-3 As R(f) is in the continuous form, circular correlation can be determined as follows:

$$C(n) = IFFT\{FFT(S(n)) \times conj(R(n)\} \tag{2.9}$$

Step-4 Finally, through the circular correlation information, f_{DC} is estimated as:

$$f_{\text{DC}}^{EB} = \frac{N_{\text{DC}}}{N} \times PRF \tag{2.10}$$

In above equation N_{DC} is zero crossing point of circular correlation, while N belongs to length of azimuth data.

2.1.4 Ocean Surface Current (OSC) Retrieval

The OSC is derived from f_{DC}, incident angle θ, and wave number k_r, given by [9]:

$$U_D = -\frac{\pi f_{\text{DC}}(\eta, \tau)}{k_r \sin\theta} \tag{2.11}$$

while calculated value of k_r is 113.28 m^{-1} for Sentinel-1.

2.2 Results and Conclusion

Experiments were conducted to evaluate the CDE, SDE, and EB techniques, compare their performance, and subsequently derive ocean surface currents based on the estimated f_{DC} history. Sentinel-1 SAR data with SM mode and VH-polarization was utilized for this task. A 2D sliding window of 64×64 pixels is used to estimate f_{DC} with the help

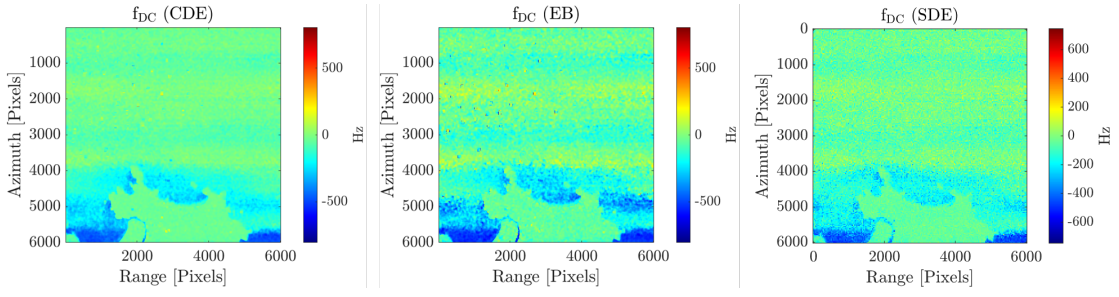

Figure. 2.1 Signature of Doppler centroid for given SAR scene obtained by CDE, EB, and SDE methods.

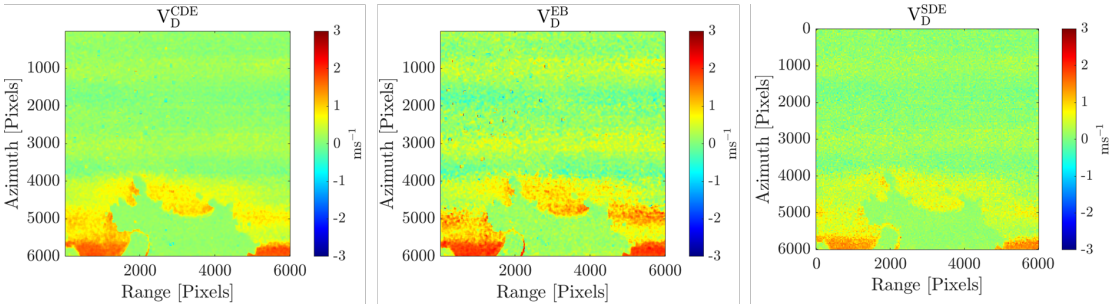

Figure. 2.2 Retrieved ocean surface current based on Doppler Centroid given in Fig. 2.1.

of a 2D convolution filter. The results are confined to the primitive baseband range (±PRF/2). The positive values indicate that the Doppler is moving toward the platform. The f_{DC} of moving ships in the given SAR scene alters the homogeneity of the Doppler due to spectrum balancing since the back-scattered values of point targets (like ships) are greater compared to ocean water pixels. Ocean surface currents are retrieved from f_{DC} history and the range of incident angles. The current fluctuates up to 3 m/sec, depending on the Doppler's nature. However, the (+ and -) signs depend on the f_{DC} information. The current values are altered in the EB method due to the presence of obvious moving targets in the SAR scene, as can be noticed in Fig. 2.2(b). Based on the given experiments, it is important to note that while both CDE and SDE perform well for distributed and non-homogeneous scenes, the EB method demonstrates favorable performance primarily in homogeneous scenes.

Three SOA techniques are implemented to estimate f_{DC} to extract ocean surface current, and comparing their performance numerically. The CDE, and SDE methods achieve a stable f_{DC} within the primitive baseband range (±PRF⁄2). The difference between all methods is dramatic for a reason: the EB method dominates f_{DC} due to the presence of point targets in the scene. It is concluded that, for distributed and non-homogeneous SAR scenes, both CDE and SDE perform very well, and the EB method performs nicely either for point targets or homogeneous scenes. Its estimation decreases when homogeneity is destroyed in a scene with prominent point targets.

Chapter 3

De-ramping of TOPS Data and CV Network to Preserve SAR Properties

The spectral characteristics of a single-look complex interferometric wide (SLC-IW) swath and terrain observation by progressive scan (TOPS) are significantly different from those of a strip-map (SM). In TOPS mode, phase information is preserved, and without de-ramping, ramps appear for the components extracted from azimuth information, namely the f_{DC}. Therefore, a solution is required to overcome this issue while exploiting TOPS SAR data. To eliminate the phase term, a chirp signal is generated for the purpose of de-ramping. The method for de-ramping is then discussed, proposing an efficient utilization of the SNAP tool to achieve this goal.

3.1 On the De-ramping of TOPS SAR data

To extract the preserved phase term, it is essential to move spectral component of SLC-IW to baseband. The phase term needs to be multiplied in time domain with the SLC signal S_{SLC}. The phase term for de-ramping is defined as:

$$\phi(\eta,\tau) = \exp\{(-\mathrm{j}\pi \mathrm{k_t}(\tau))(\eta - \eta_{\mathrm{ref}}(\tau))^2\} \tag{3.1}$$

where, reference time $\eta_{\mathrm{ref}}(\tau)$, and Doppler centroid rate $k_t(\tau)$ are function of range samples. After evaluation of necessary parameters, de-ramping to cancel quadratic drift can be achieved by simply multiplying phase term with SLC signal.

$$S_d(\eta,\tau) = S_{SLC} \times \phi(\eta,\tau) \tag{3.2}$$

The ramps from TOPS data are eliminated using a chirp signal, resulting in the acquisition of baseband data as depicted in Fig. 3.1 (a).

Alternatively, de-ramping can be achieved in the SNAP tool using the Sentinel-1 TOPS operator [5]. The complete step-by-step methodology is presented in Fig. 3.1 (b). As

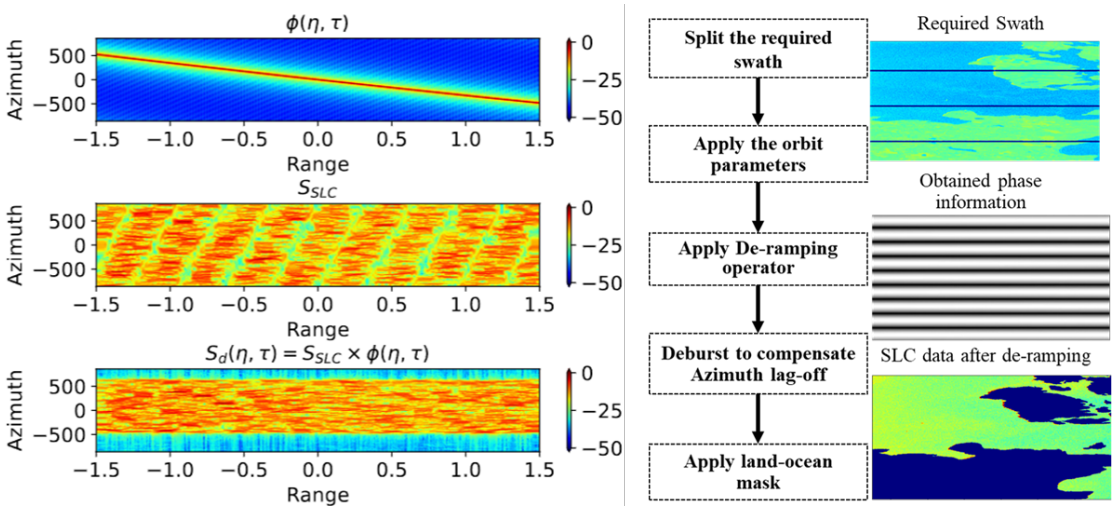

Figure. 3.1 (a) De-ramping by using ESA method. (b) De-ramping by using SNAP tool.

TOPS consists of multiple swaths, first split the required swath and apply "deramp-demod" operator. To compensate the azimuth null spacing (to avoid residual ramps) between each burst, the operator "deburst" greatly helps in achieving a refined scene and removing stripes that impede feature extraction. As the main focus is solely on ocean Doppler parameter estimation, the SNAP tool assists in masking out the land area, thereby enhancing the accuracy of our estimates. The land-ocean mask is applied to avoid Doppler effect caused by dynamic objects present on the land.

The ocean circulation parameters in this chapter are extracted from complex SAR data that are data-driven, whereas the parameters in the benchmark/reference are predicted from ocean product (OCN) information and based on the polynomials given in the metadata . Doppler centroid f_{DC} and OSC estimation are given in chapter-2. Thus, OSC is used to retrieve significant wave height (SWH) in image domain based on empirical relationship given as:

$$\mathbf{H_S} = 4\sqrt{\frac{1}{T}\sum_{i=1}^{T}(U_D^{(i)})^2} \tag{3.3}$$

where, $\mathbf{H_S}$ is an important parameter for seashore engineering. The SWH is the average wave height in a given period of time T, which is the azimuth time span of data under observation.

The de-ramping is done so far to eliminate quadratic drift of phase term by chirp signal or using SNAP tool. When phase term $\phi(\eta,\tau)$ is multiplied with original SLC signal S_{SLC} the data moves to baseband domain, as shown at the bottom of Fig. 3.1. The ocean circulation parameters include OSC and, SWH. The OSC is evaluated using f_{DC} estimated by the CDE method, which perfectly matches the benchmark data shown in Fig. 3.2 The RSV is in a good match and reaching up to 2.5 m/s in the core of the stream. The surface velocity on the ground is zero as land is masked and paving zero doppler. The reasonable parameter estimates demonstrating the efficacy and necessity

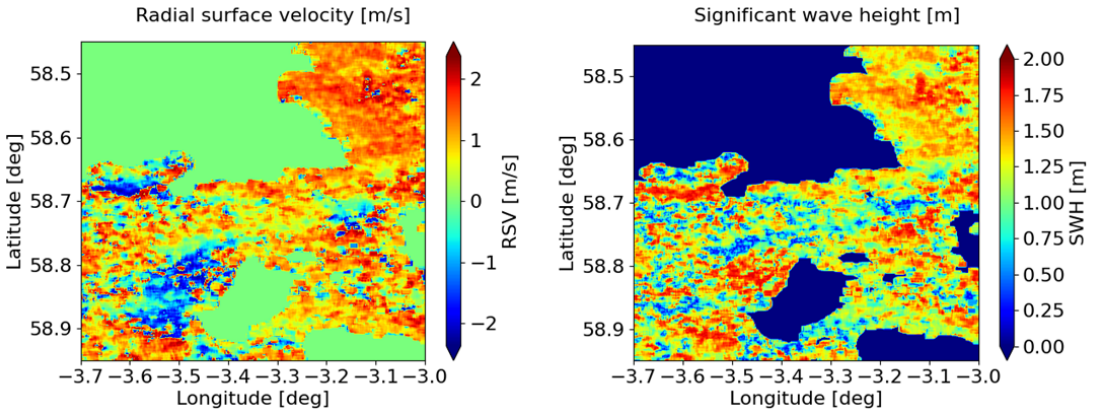

Figure. 3.2 OSC (m/s) derived from data-driven Doppler centroid (b) SWH (m) derived from RSV.

of de-ramping for the SLC-IW TOPS data. The error estimation lacks in this part, and some physical parameter remain to be investigated regarding ocean current field, which will be carried out in subsequent section of this chapter.

3.2 CV network for TOPS SAR data Preservation

The applications of the deep learning is increasing rapidly. Development of the Complex-Valued (CV) networks that can process CV data has opened a lot of opportunities for utilizing the immense capabilities of deep networks for CV data, including Synthetic Aperture Radar (SAR). The competency of the CV deep architectures for preserving the properties of the original SAR data and how it affects the physical parameter's retrieval is evaluated in this section. The obtained OSCs are compared to demonstrate the ability of the CV deep architectures to learn the data model and preserve the original Doppler information in SAR data.

A fully CV network is used in this study to reconstruct the CV SAR images. All the layers in this network, including the convolutional, pooling, and batch normalization layers, are in the complex domain. Moreover, the weights and biases in the neurons, and the activation functions are complex-valued. Furthermore, a CV backpropagation, based on stochastic gradient descent, is used for training the CV autoencoder. However, the loss function remains in the real domain to minimize the empirical issues [10].

All the mathematical operations in the CV network are performed in the complex domain. For instance, the convolutional layer, which is an important component of deep networks and is used in various deep architectures to extract discriminant latent features from the input data, is applied in the complex domain. The output of the convolution, $y_i^{(l+1)} \in \mathbb{C}^{W_2 \times H_2 \times l}$ is computed by the convolution between the input feature map from the previous layer, $X_{iC}^{l} \in \mathbb{C}^{(W_1 \times H_1 \times C)}$, and the weights of the neurons, $w_{iC}^{(l+1)} \in \mathbb{C}^{F \times F \times C \times l}$, and then adding a bias, $b_i^{(l+1)} \in \mathbb{C}^{l}$.

In order to train the CV network, the Wirtinger calculus is used to perform the backpropagation in the complex domain [11]. According the the Wirtinger calculus, the partial derivatives of a complex function $f(z)$ with respect to the complex variable $z = x + jy \in \mathbb{C},\ (x,y) \in \mathbb{R}^2$. The architecture of the developed CV autoencoder consists of two main parts, an encoder and a decoder. The encoder is used to encode the input SAR image and create the bottleneck embedded features. Later, the decoder part reconstructs the CV-SAR image from the embedded features. The skip connections between the encoder and decoder are used to reduce the risk of degradation in the deep network and ensure an uninterrupted flow of the gradients in the network [12]. Both of the polarization channels of the CV-SAR data are fed into the network as patches of 100×100 pixels. The CV network reconstructs both of the polarization channels at the same time.

We evaluate the performance of the CV autoencoder and its ability to preserve the original Doppler centroid information. The CV autoencoder, trained in [12], Sentinel-1 StripMap (SM) mode data with HH and HV polarization channels (Different from the dataset used in this study) is used. The de-ramped IW data with VV and VH polarization channels is reconstructed with the trained network. The results from this experiment are annotated as reconstructed (R).

The network is retrained, using the SLC-IW TOPS SAR data with VV and VH polarization channels. The network is trained for 10 epochs, with batch size 10, learning rate 0.001 and Mean Square Error (MSE) loss function with 90% of the data as the training set. Later the retrained network is used to reconstruct the IW data with VV and VH polarization channel (similar to the training data). The results from this experiment are annotated as reconstructed-Trained (RT). Based on our experiments the VH polarization channel is better for OSC estimation. After reconstruction of the CV-SAR data with the CV autoencoder, the Correlation Doppler Estimation (CDE) method is used to estimate f_{DC} and retrieve the OSC. The land is masked out using SNAP tool so that not to search for Doppler on land. Nevertheless, the spatial resolution and limits are consistent in all three experiments to visually observe variation in the estimated OSC signatures.

The f_{DC} and OSC estimated from the original SAR data annotated with O, the reconstructed SAR data from the [12] network annotated with R, and the reconstructed SAR data from the retrained network annotated with RT are shown in Fig. 3.3. Comparing the f_{DC} and OSC estimated from the [12] network (Fig.3.3 (b) and (e)) with the original SAR data (Fig. 3.3 (a) and (d)), a noticeable difference in the estimated ocean circulation parameter is visible. The reconstructed CV SAR data, despite having the similar OSC pattern, tends to estimate lower values for the current and weaker Doppler. However, when the CV autoencoder is retrained using the SLC-IW TOPS SAR data, the estimated f_{DC} and OSC (Fig.3.3 (c) and (f)) show a very high resemblance with the results from the original SAR data. The high resemblance between the ocean circulation parameter's estimation in the original and the reconstructed SAR data demonstrates that the CV autoencoder has preserved the SAR data model even without retraining (experiment

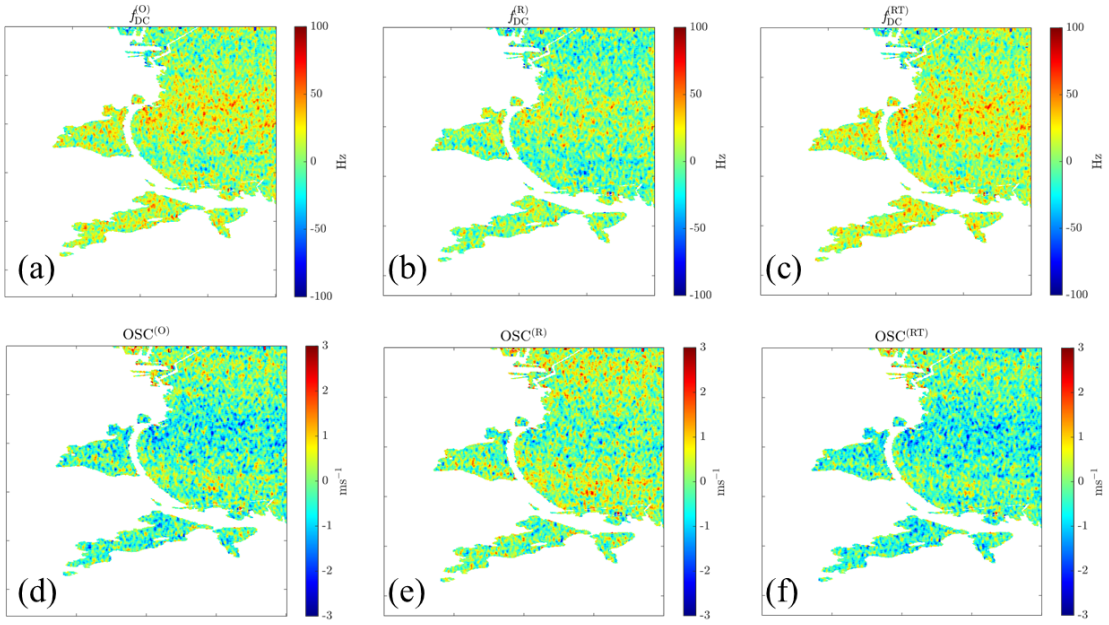

Figure. 3.3 (a), (b), and (c) calculated f_{DC} over the study area and (d), (e), and (f) estimated OSC from the Original (O), Reconstructed with the [12] network (R), and Reconstructed with the retrained network (RT) SAR images, respectively.

annotated with R). Obviously, retraining the network with the similar type of the data (IW and VV-VH Polarization channels) has improved the performance of the CV autoencoder significantly.

In this study, the competence of the CV auto-encoders to preserve the original properties and the physical model of the CV-SAR data and how it influences the physical parameter's retrieval from these data is evaluated. To this end, a CV autoencoder is trained to reconstruct the CV-SAR images and the f_{DC} and OSC parameters extracted from the original and reconstructed SAR data. The comparison between the obtained parameters demonstrated that the CV autoencoder successfully learned the SAR data model and preserved the original Doppler centroid information to a good extent.

Chapter 4

Polarimetric SAR Data for Target Detection Based on CFAR

Coastline extraction, marine-time target or traffic monitoring, and ice-cover delineation by exploiting optical images are challenging during adverse weather conditions. As a matter of fact, collecting *in-situ* data is expensive and not always possible. Consequently, CFAR approaches have a versatile scope for SAR-based target identification. The matrix for target delineation (i.e., $f_{\mathrm{DC}}, \sigma^0,$ and ρ) undergoes an ensemble averaging process, following which the CFAR technique is applied to determine the threshold value essential for distinguishing between target and non-target entities. Subsequently, an image processing block is employed to precisely quantify the boundaries or edges of the desired targets.

4.1 Coastline Extraction using f_{DC} Images

A novel coastline extraction method is proposed based on classic coastal dynamic variation, such as f_{DC}, since coastline is static and has zero Doppler with respect to the dynamic sea-state. The Doppler parameter is used to delineate coastlines when neither *in-situ* data nor cloud-free optical images are available. The results of the Doppler-based novel technique allow us to investigate the impact of natural hazards on coastline degradation [6].

The overall impression is that the coastline is static with respect to the sea and paves zero doppler rate theoretically. Thus, dynamic and static natures easily distinguish the water and land. The f_{DC} is estimated by our CDE method given in Chapter 2. By using the sliding window 'w' of size 9×9 locally computed f_{DC}. The next step is to extract the coastline while enhancing the land and water separation. Estimated f_{DC} is set to its absolute values for the sake of simplicity to use a single threshold value $|f_{\mathrm{DC}}^{[VH]}| = |f_{\mathrm{DC}}(\eta, \tau)|$. The CFAR method is applied over ROI which intends to provide a hetero-logical image from $f_{\mathrm{DC}}^{[VH]}$ at 2σ to clearly discriminate between land and sea.

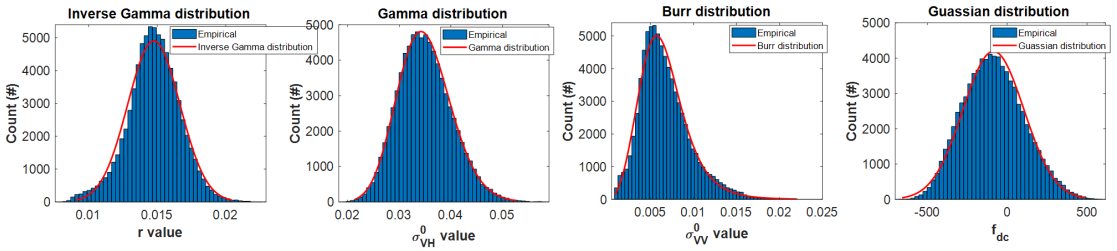

Figure. 4.1 For gien dataset, r_c, σ_{pq}, σ_{qq}, and f_{DC}, closely follow Gaussian, inverse Gamma, Gamma, and Burr distributions respectively.

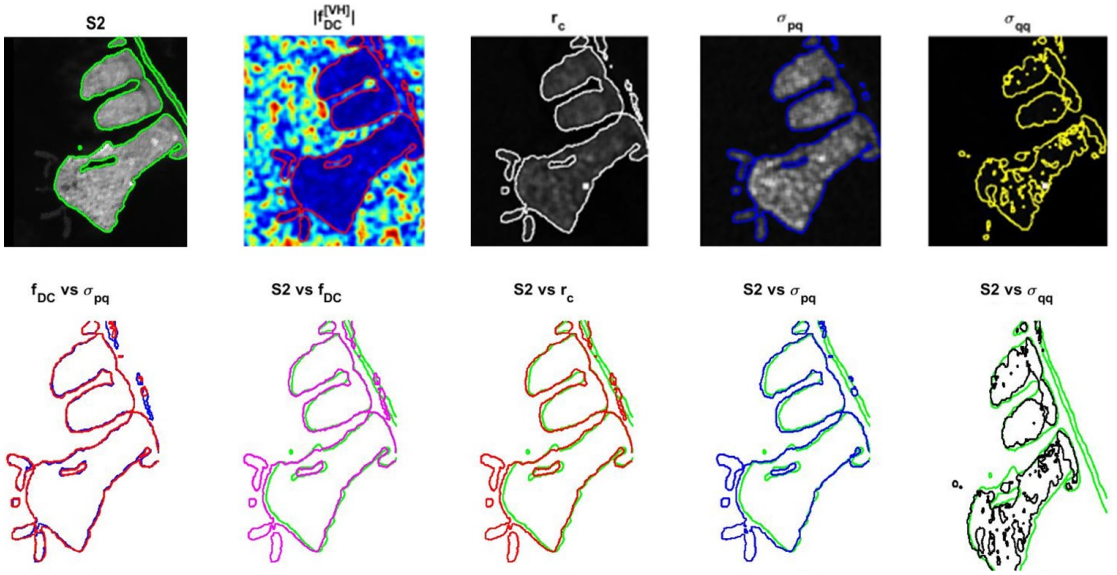

Figure. 4.2 Row one represents extracted coastline maps of Sentinel-2 (S2), $|f_{\mathrm{DC}}^{VH}|$, r_c, σ_{pq}, and σ_{qq} with their respective imagery over ROI related to the scene collected. Coastline map of S2 (green) is overlapped with $|f_{\mathrm{DC}}^{VH}|$ (magnetic), r_c (red), σ_{pq} (blue), and σ_{qq} (black) as shown row-2.

For comparison, coastline extraction is carried out using SOA the correlation matrices including dual-pol, co-pol and cross-pol, ($r_c = \langle |S_{VH}| \cdot |S_{VV}| \rangle$, $\sigma_{pq} = \langle |S_{VH}|^2 \rangle$, $\sigma_{qq} = \langle |S_{VV}|^2 \rangle$). The given relationships follow Inverse Gamma, Gamma, Burr and Gaussian distributions to obtain threshold using CFAR method as shown in Fig 4.1 [13].

The estimated $|f_{\mathrm{DC}}|$ is influenced by dynamic bragg waves, and medium scale variations. The empirical distribution for f_{DC} over the smooth water region is overlapped with theoretical Gaussian distribution. However, for the different estimation matrix and sea-state conditions the value of threshold 'T_{CFAR}' and distribution both vary from data to data. There exist false alarms after applying 'T_{CFAR}' in fact few pixels on the ocean area have zero Doppler, so to discard these false alarms it involves former approach σ_{pq} to filter out zero Doppler pixels over water. This criterion was chosen to isolate the variation caused by the sea dynamics and effectively extract the coastline.

The detected coastline maps based on the above experiments are given in Fig. 4.2. The maps of coastline obtained from $|f_{\mathrm{DC}}^{VH}|$,r_c, and σ_{pq}, having minimal variation with similar maps, besides σ_{qq} maps are erroneous due to the impact of lower incidence angle.

Table 4.1 Quantitative analysis based on overall agreement (OA)

Comparison / OA	S2 vs $\lvert f_{DC}^{VH} \rvert$	S2 vs r_c	S2 vs σ_{pq}	S2 vs σ_{qq}
Land	0.3414	0.3418	0.3447	0.2524
Water	0.5799	0.5792	0.5693	0.6294
Land + Water	**0.9214**	0.9210	0.9140	0.8818

The extracted coastline maps of proposed $|f_{\mathrm{DC}}^{VH}|$ and σ_{pq} one of the SOA method in red and blue colors, respectively, are overlapped to quantify the accuracy of two methods, and a good agreement can be observed. Sentinel-2 (S2) image accurately detect the coastline and small water target, coastline map is highlighted with green color given in Fig. 4.2 row one. To quantify the performance, the overall agreement (OA) is computed between S2 and both the proposed and SOA methods as given in Table 4.1 [14]. The total number pixel classified as sea, land, and both sea + land. Experimental values of pixel classification for land and sea both together, show that $|f_{\mathrm{DC}}^{VH}|$ performs robust as r_c, σ_{pq}, however, σ_{pq} is under influence of incidence angle.

The impacts ocean circulation parameters on the coastline's structure are described. The datasets are collected at various intervals to accurately predict the impact of Doppler parameters on coastlines. Variations in physical structures are observed on the coastlines. The coastlines from two different dates shows that coastline is facing cuts and the sea state is slightly rough, which is an impact of high Doppler parameters.

4.2 Sub-Aperture Decomposition for Ship Detection

The contrast between ship targets and the surrounding sea can be improved in SAR images by splitting bandwidth in the sub-apertures (SAs) to attain high azimuth resolution. This section describes SA decomposition for the detection of moving ships. The proposed dual-pol SAs averaging method employs the CFAR approach followed by the statistical Gamma (Γ) distribution to determine the threshold value for distinguishing ships and water. Furthermore, the ship's velocity parameter in the azimuthal direction is estimated based on SAs displacement.

To achieve high azimuth resolution, the SA replaces the real antenna aperture by processing the signal along the azimuth dimension. The concept of SD generates SA images synthetically, which further optimize object detection [15]. The produced SAs are averaged for both polarizations for ship detection. The modulus of the unnormalized correlation between co-pol and cross-pol channels is defined by correlation matrix $r = \langle |S'_{\mathrm{VH}}| \cdot |S'_{\mathrm{VV}}| \rangle$, given that; $S'_{\mathrm{VH}} = \frac{1}{\mathrm{N}} \sum_i^{\mathrm{N}} S_{\mathrm{VH}}^{(i)}$, and $S'_{\mathrm{VV}} = \frac{1}{\mathrm{N}} \sum_i^{\mathrm{N}} S_{\mathrm{VV}}^{(i)}$. Where S' represents averaging of SAs for each polarization, N is number of SAs.

The framework of the automatic ship detection algorithm uses CFAR approach, the empirical distribution of smooth water is overlapped with theoretical distribution. The generalized Gamma well approximates the empirical statistical distribution of r. The purpose of developing automatic threshold detectors is to keep the probability of a false alarm constant. Threshold, $T_{\mathrm{CFAR}} = \Gamma(1 - P_{\mathrm{fa}}, \frac{\mu^2}{\sigma^2}, \frac{\mu}{\sigma^2})$, where μ, and σ are the non-negative scaling parameter, and standard deviation respectively. The probability of false alarm ($P_{\mathrm{fa}} = 10^{-6}$) for the estimation of T_{CFAR} is given as: $P_{\mathrm{fa}} = \int_0^{T_{\mathrm{CFAR}}} \mathrm{PDF}(r^{(w)})\mathrm{dr}$, where $r^{(w)}$ represents water clutter. Once the logical image is obtained, the pixel-by-pixel ship target is extracted using the sobel edge detection algorithm.

The ship velocity is obtained with the SA displacement method, which utilizes the peak correlation value and pixel displacement, given as; $V_S = \sum_{i=1}^{N} \frac{r_i \Delta_x^i S_{\mathrm{Azi}}}{T_{\mathrm{SA}}} / \sum_{i=1}^{N} r_i$, where r_i is the cross correlation of two SAs, T_{SA} is synthetic aperture time, and Δ_x^i is displacement in azimuth where S_{Azi} presents its pixel spacing. The SAR aperture, divided into three SAs, is reconstructed using three Hamming windows $h(w)$; therefore, the SD produces multiple SAs from the original SAR. The SAs are averaged in their respective polarizations, and a dual-pol correlation metric 'r' is adapted for ship detection, as shown in Fig. 4.3(a). The empirical distribution of the r image is overlapped with theoretical gamma (Γ) distribution, as shown in Fig. 4.3(b). Then, the obtained value of T_{CFAR} discriminated between the sea and ship to display in the form of a binary image, as shown in Fig. 4.3(c). Finally, the Sobel edge detector provides boundaries to identify ships and water boundaries, and by overlapping an amplitude image and the overall extraction results, the detected ships are shown in yellow in Fig. 4.3(d).

Eigenvalues ($\lambda = \sum_{i=1}^{2} p_i \lambda_i$) provide the total size or canopy information of the target. Therefore, the ship size obtained by the proposed SAs averaging method is compared with λ to estimate the accuracy of both methods, as shown in Fig. 4.3(e). The ship sizes obtained from the Eigen value (in blue) are compared with the proposed approach (in red). Both techniques provide approximately reliable ship sizes with 90% accuracy. Displacement in SAs does not impact actual sizes, but the choice of window size does.

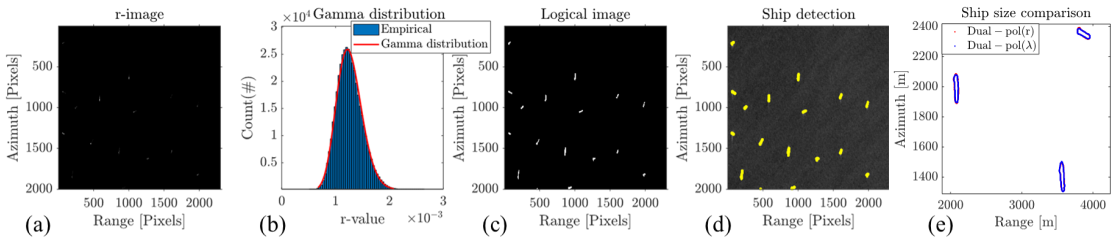

Figure. 4.3 (a) r-image, (b) empirical and theoretical distribution of water region, (c) binary image to discriminate between ship and water, (d) ship detection result of the overall method, and (e) comparison of ship size obtained by λ and r-image.

4.3 Ice-cover Delineation using SAR and Optical Data

Remotely sensed satellite imagery plays an important role for the monitoring of glaciers and ice sheets that are difficult to observe from the ground because of their huge magnitude and severe environmental conditions. SAR is a reliable source for ice monitoring because of its frequent revisit times. Therefore, this section focuses on an unsupervised method for extracting ice cover by exploiting dual-pol Sentinel-1 ground-detected SAR data over Devon Island, which is surrounded by oceans. A CFAR detector was adapted with the theoretical "Burr" distribution to derive the CFAR threshold value to delineate the ice cover. The ice-cover extraction accuracy of the proposed matrix and the SOA single-pol matrix were meticulously compared with the ice cover detected by Sentinel-2 data.

Data preprocessing was excluded to determine the effectiveness of the method. Dual-pol SAR data with a correlation metric (ρ) is used for ice cover detection given as: $\rho = \langle S_{\mathrm{HV}} \cdot S_{\mathrm{HH}} \rangle$. Speckle noise can be reduced by spatial filtering. Therefore, using a sliding window of size 15×15 to locally compute the ensemble averaging of spatial information, where $\langle \cdot \rangle$ is the spatial mean filter. Subsequent step is to search for the empirical distribution across the ice region to align with the theoretical distribution. The CFAR threshold is calculated from the patch of ice region as the probability PDF of the Burr distribution (β), as follows: $T_{\mathrm{CFAR}} = \beta[P_{\mathrm{fa}}^{-\frac{1}{\alpha}} - 1])^{\frac{1}{\mu}}$, where μ and α are non-negative shape parameters, and β is a non-negative scale parameter. Probability of a false alarm (P_{fa}) for the estimation of T_{CFAR} based on Burr distribution is given as; $P_{\mathrm{fa}} = \int_{T_{\mathrm{CFAR}}}^{\infty} \frac{\alpha\beta^{\alpha}\mu\rho_i^{(\mu-1)}}{(\beta+\rho_i^{\mu})^{\alpha+1}} d\rho,\ \rho > 0$, where ρ_i represents the ice clutter. Hence, the T_{CFAR} value correctly discriminate ice and non-ice targets. Once the logical image I_{L} is obtained, the pixel-by-pixel targeted ice is extracted using the Canny edge detection algorithm. The results are compared with co- and cross-polarized correlation matrices, namely $\sigma_{\mathrm{HH}} = \langle S_{\mathrm{HH}} \cdot S_{\mathrm{HH}} \rangle$ and $\sigma_{\mathrm{HV}} = \langle S_{\mathrm{HV}} \cdot S_{\mathrm{HV}} \rangle$ respectively [16]. When comparing the results with *in situ* data, and two types of data have different resolutions, to facilitate a meaningful comparison, a co-registration method has been developed in the SNAP toolbox to align both data products to the same resolution.

The application of this research is ice-retreat estimation. To estimate the velocity or retreat of ice cover between two different dates, two points are selected. First, the point of the first ice line that is farthest from the second line is selected, and the distance between these two points is measured in meters. Second, the point of the second ice line closest to the first line is selected, and the distance between these two points is measured in meters. Finally, calculate the retreat by dividing the Euclidean displacement by time span (day). The retreat velocity V_R is given by:

$$V_R = \frac{||X_C - X_F||}{T_S} = \frac{\sqrt{(X_{C1} - X_{C2})^2 + (X_{F1} - X_{F2})^2}}{T_S} \tag{4.1}$$

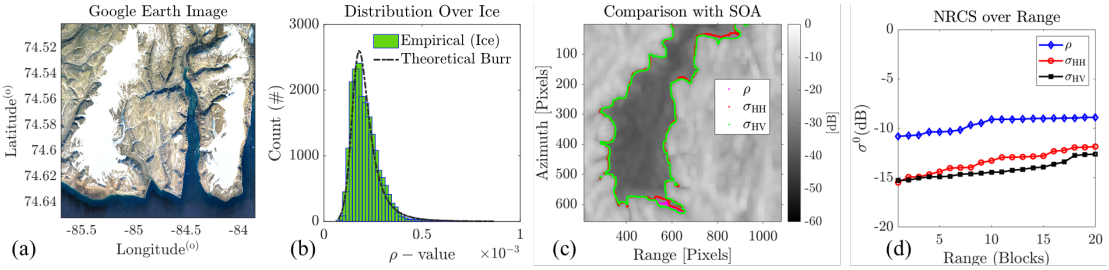

Figure. 4.4 (a) Google Earth image view of given ice cover. (b) Empirical distribution of ice overlapped with the theoretical Burr distribution. (c) Ice-cover detected by ρ, σ_{HH}, and σ_{HV}, and (d) NRCS of the given matrices, where the proposed matrix showed an improved NRCS for better ice cover extraction.

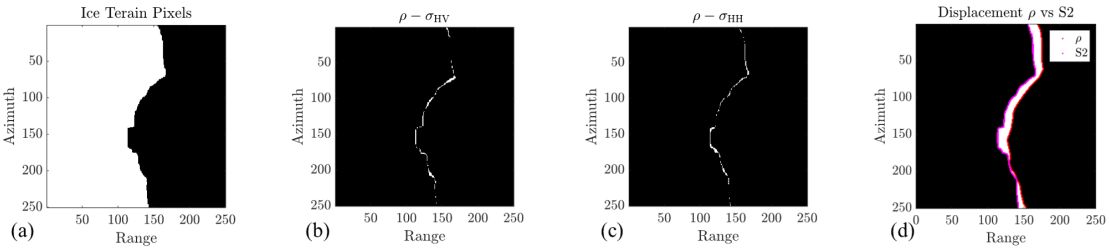

Figure. 4.5 Homogeneous patch of Ice and terrain pixels to quantify accuracy of each matrices (b) $\rho - \sigma_{\mathrm{HV}}$ (c) $\rho - \sigma_{\mathrm{HH}}$, and (d) $\rho - \mathrm{S2}$.

where X_C, X_F, and T_S are the closest points on ice line 1, the farthest points on ice line 2, and the time span per day, respectively. The methodology is tailored to handle the unique characteristics of the clutter present in ice- or ice-infested bodies. The empirical and theoretical distributions were derived from an ice region, providing insight into the statistical properties of the data. The ice region paves the burr distribution; therefore, CFAR for this distribution was implemented. The ice cover was delineated with great precision using the proposed method with S1 SAR data, as shown in row-1 of Fig. 4.4. In contrast, Fig 4.4 (a). Google earth image shows a sheet of the ice that is obtained across Devon Iceland. Fig 4.4 (b) presents the empirical distribution followed by theoretical Burr distribution over ice region to extract Ice-cover. Fig 4.4 (c) shows ice cover extracted using ρ, σ_{HH}, and σ_{HV}, the ice edges are quantified by the Canny edge detector and overlaid geocoded image to illustrate the overall process. The NRCS plots for each matrices are given in Fig 4.4 (d), where ρ shows an improved NRCS.

A patch of ice (white) and terrain (black) pixels in Fig. 4.5(a) quantifies matrix accuracy. In (b), ice-terrain line differences are shown for ρ and σ_{HV}, while (c) displays them for ρ and σ_{HH}. This variation arises from different matrices. Yet, (d) highlights a distinct S1 (magenta) to S2 (red) displacement, linked to dataset time difference, offering a retreat velocity estimation opportunity.

Chapter 5

Inverse SAR Image Reconstruction and Sparse Feature Extraction

With the advancement of radar technology, imaging has become an important function of radars. Inverse synthetic aperture radar (ISAR) technology provides images of objects that are rotated with respect to the radar. This chapter encompasses three distinct applications: ISAR imaging, sparse feature extraction, and CS-ISAR imaging [1, 3].

5.1 ISAR Imaging Assessment

A monostatic model of ISAR was deployed to collect radar backscattering data in the millimeter (mm) wave band (67–110 GHz) using targets with circular, rectangular, and non-canonical shapes. The ISAR experiments were performed to assess the imaging performance of the three methods, including wave-number ($\omega - k$), spherical wavefront compensation, and back-projection. To evaluate the methods, we calculated the point spread function (PSF) for the mm-wave wire's impulse response. There is a trade-off: the $\omega - k$ domain loses resolution compared to the SWFC and BP methods but can obtain a satisfactory image at a lower computational cost [17].

The modified $\omega - k$ method is computationally efficient because it uses a built-in function for 2D interpolation and an inverse Fast Fourier Transform (FFT) [18]. The interpolation process removes range cell migration (RCM) and range-azimuth coupling.

$$\text{ISAR}_{\omega-k} = \sum_{i}^{N} \text{interp2}(\left[K_{X,Y}\right],\ S_h(\omega,k),\ \left[K_{r,\theta}\right]) \tag{5.1}$$

where K_X and K_Y are grid dimensions, S_h is pre-processed ISAR data, and $K_{r,\ \theta}$ is polar transformation function.

In the SWFC method, the data from all turntable angles is gathered to compensate for the wave fronts. The SWFC is given as; $S_\psi = \sqrt{(R\cos\phi\cos\theta + X)^2 + (R\cos\phi\sin\theta + Y)^2}$, where ϕ is the incidence angle between radar and target 'R' is the distance from target to

radar. $X,$ and Y are elements of a predefined 2D grid. The final complex ISAR image is:

$$\text{ISAR}_{\text{SWFC}} = \int_0^{\infty} \int_{-\pi}^{+\pi} S_h(f,\theta) \exp\left(2jk \times S_\psi\right) df d\theta \tag{5.2}$$

where $k = \frac{2\pi f_{\text{vec}}}{c}$, and f_{vec} is the frequency vector for a given range of bandwidth, and f denotes data samples.

The core idea of the BP approach is to subtract the distance between the radar and the target and compensate for it in terms of the phase for coherent accumulation, avoiding the distance migration: $S(x,y) = \int_y \int_x f(x,y) \exp\left(-j2kR(x\sin\theta - y\cos\theta)\right) dxdy$. Where, $f(x,y)$ is the function of range-compressed raw data.
Given that, $S_\zeta = \sqrt{(R\cos\phi\cos\theta - X)^2 + (R\cos\phi\sin\theta - Y)^2}$ is the distance compensation in terms of phase between radar and the image grid. The back-projected ISAR image is given as:

$$\text{ISAR}_{\text{BP}} = \int_x \text{Interp1}\left(\left[K_{X,Y}\right], f_h(x,y), S_\zeta\right) * \exp\left(-j\frac{4\pi f_{\text{vec}}}{c} \times S_\zeta\right) dx \tag{5.3}$$

The capabilities of ISAR methods are expressed in terms of "*Point Spread Function*" (PSF), utilizing the impulse response of a mm-wave wire coupled between the radar and the processing unit. Nevertheless, the PSF is the reconstructed image of a single scatterer (wire) located at the origin of the coordinate system. This compare the capabilities of the

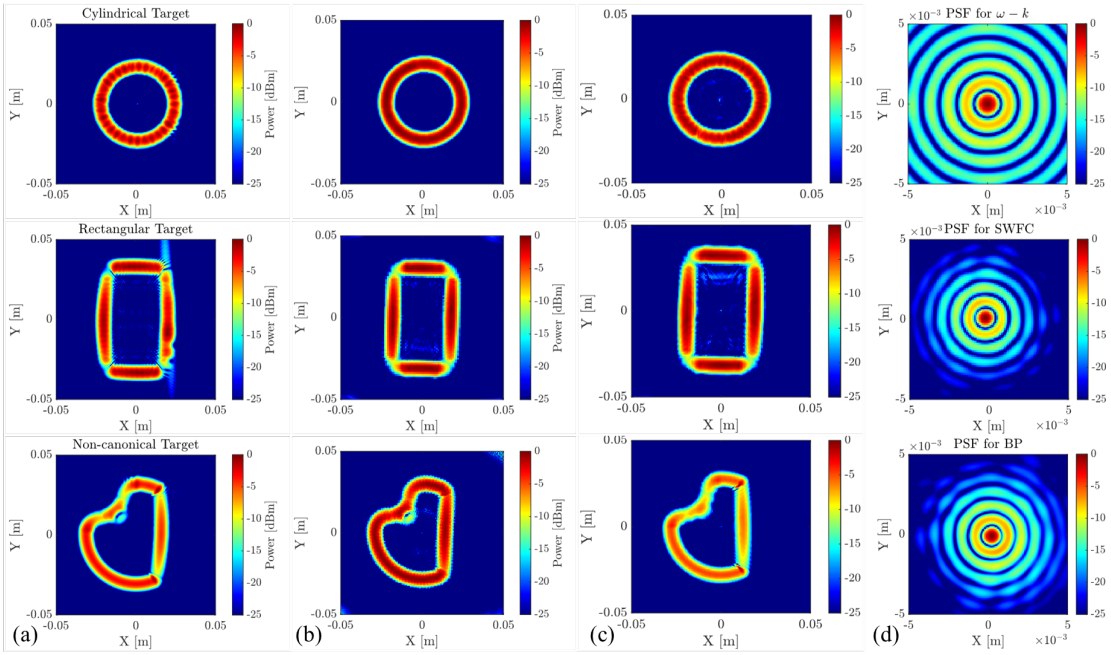

Figure. 5.1 The imaging results of Cylindrical, Rectangular, and Non-canonical targets. (a) presents the results obtained using the $\omega - k$ method, (b) presents the results obtained using the SWFC method, and (c) validates the results attained by BP method. (d) The -25 dB PSF images for the IR of mm-wire for $\omega - k$ domain, SWFC, and BP methods.

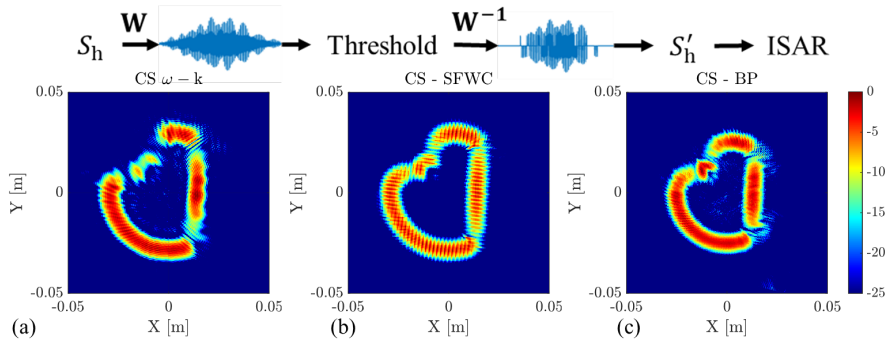

Figure. 5.2 ISAR images obtained with 70% of the data (compressed or sparse at 30%) after a thresholded 2D-DWD. (a) $\omega - k$, (b) SWFC, and (c) BP.

implemented methods to achieve sub-millimeter spatial resolutions. Moreover, the ability of the aforementioned ISAR methods to handle compressible data was evaluated. The 2D discrete wavelet decomposition (2D-DWD) is applied to make the data compressible in both the range and cross-range dimensions by reducing dimensionality [19].

The imaging results for $\omega - k$ method are shown in column (a) of Fig. 5.1. The imaging results are in close correspondence with the ground truth in terms of size and shape. The $\omega - k$ method has an effective ISAR image reconstruction that remains independent of the target-to-radar distance. In particular, compared to the traditional SWFC and BP algorithms, as shown in Fig. 5.1 columns (b) and (c), the number of incorrectly reconstructed points was reduced. The PSF images of the SWFC and BP methods have perfect concentrations at the center, as shown in Fig. 5.1 column (d). The imaging was focused with respect to the center, and the side lobes were rapidly reduced.

In contrast, the PSF image of the $\omega - k$ domain shows relatively high side-lobe values. However, millimeter-wave imaging, with a lower computational cost and ample resolution, has great potential for object detection in various fields. Fig. 5.2 presents the results of the performance analysis of ISAR imaging for a complex non-canonical target using 30% compressed or sparse data obtained after 2D-DWD. This shows $\omega - k$ drops in imaging because of the mitigation of useful coherent processing intervals (CPIs) as compared to SFWC and BP. However, by applying any CS technique, the resolution can be restored, resulting in a better-focused, super-resolved image compared to this one.

5.2 Scattering Properties Estimation of ISAR Images

The dual-pol decomposition technique enables precise retrieval of scattering mechanisms (H-α), allowing for various applications. A novel case study of 2D ISAR images for scattering property estimation was presented. Eigenvector descriptors were employed to identify the scattering mechanism based on the Lee and Pottier H-α plane. This mechanism was presented for the first time in the ISAR setup. Given that decomposition enhances the target characterization for studying scattering mechanisms, the application

of the Radar Vegetation Index (RVI) demonstrates how dual-polarized ISAR images can be used for vegetation identification [20].

The measurements were conducted using the experimental radar COBRA on the turntable on the Fraunhofer terrain with a quasi-mono-static setup paving VV and VH channels. The received channels are at a certain angular distance from the targets and have a certain delay that is compensated by $\Delta\tau = \frac{c \times R}{4\pi f_c}$, where R and f_c are radar to target distance and carrier frequency. The 2D ISAR imaging is attained by using the SWFC method, as discussed in Section 5.1. All turntable angles were gathered to reconstruct a 2D ISAR image. For both the polarization-focused ISAR images are S_{VV} and S_{VH}.

The coherent decomposition of dual-pol provides eigenvalues and eigenvectors of the coherence matrix [21]. The scattering vector for dual-polarized ISAR data are represented as $\mathbf{k_{Dp}} = \begin{bmatrix} S_{VV} & S_{VH} \end{bmatrix}^{\mathbf{T}}$. The 2×2 coherence matrix allows us to obtain the entropy (H), alpha (α), and span (λ) images for trees. $H - \alpha$ decomposition can be expressed by exploiting the non-negative eigenvalues (λ_i, $i = 1, 2$) and the corresponding eigenvectors, and entropy is expressed as:

$$H = -\sum_{i=1}^{2} (p_i) \log_2 (p_i), \text{where, } p_i = \frac{\lambda_i}{\lambda_1 + \lambda_2} \tag{5.4}$$

where the mean scattering angle (α) and span or mean magnitude of the mechanism (λ) are given as:

$$\alpha = \sum_{i=1}^{2} p_i \alpha_i, \text{and } \lambda = \sum_{i=1}^{2} p_i \lambda_i \tag{5.5}$$

while α, and λ provide the nature of scattering and the span or size of the target, respectively. Radar scatters are greatly influenced by vegetation type, structure, moisture, and phenology; thus, the RVI is defined, which takes these parameters into account and is very useful in vegetation monitoring at a large scale.

$$\mathrm{RVI} = \left(\frac{\langle |S_{VH}| \rangle}{\langle |S_{VV} + S_{VH}| \rangle} \right)^{1/2} \left(\frac{4 \times \langle |S_{VH}| \rangle}{\langle |S_{VV} + S_{VH}| \rangle} \right) \tag{5.6}$$

RVI is a scattering randomness measure that ranges from 0 to 1, but it is less sensitive to radar measurement geometry. For smooth surfaces, the RVI is close to zero, it increases as the vegetation grows. The RVI results are compared with DpRVI that relies on two parameters and enhances estimates. $\mathrm{DpRVI} = (1 - m_{\mathrm{Dp}} \cdot \beta),\ 0 \leq m_{\mathrm{Dp}} \leq 1$, where β is eigen value spectrum of $\mathbf{T_2}$ and m_{Dp} is degree of polarization. Fig. 5.3 upper image demonstrates the measurement setup and the turntable where tree targets are placed. Fig. 5.3 (a) shows the λ mean magnitude of the 2D ISAR images of the trees. In Fig. 5.3 (b), the higher entropy values indicate very low-amplitude backscatter, where tree canopy areas show sparse vegetation. The presence of 'α' (mean angle) values in dense leaf areas, where most values are greater than 45°, represents multiple surface scattering, as

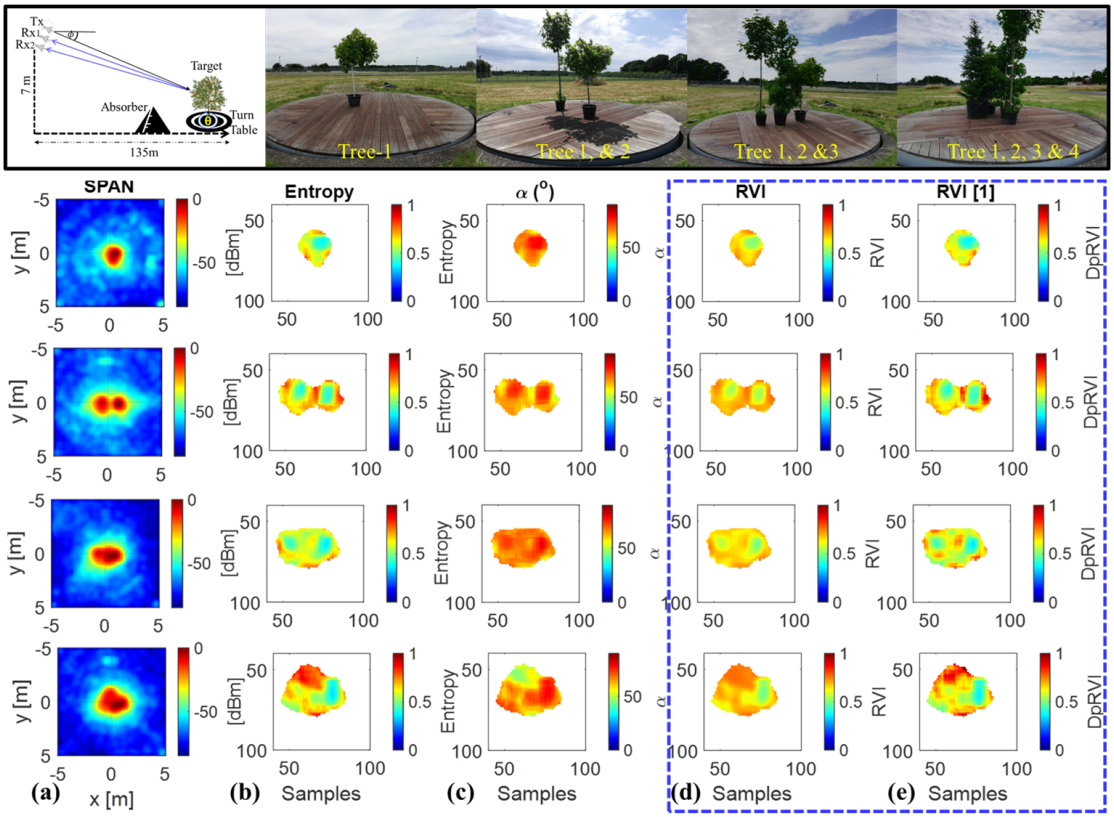

Figure. 5.3 Top row is the Geometric model and targets installed for ISAR setup. (a) ISAR imagery of trees. (b) Entropy of tree scatterings. (c) α represents the mean scattering angle. (d) Spatial signatures of RVI based on partial polarization. (e) Spatial signatures of RVI based on degree of polarization.

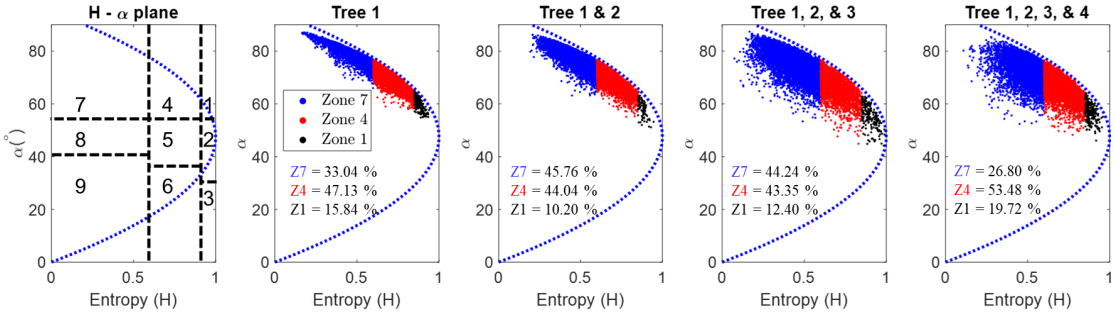

Figure. 5.4 $H - \alpha$ decomposition shows that scattering mechanism falls in zone 1, 4, and 7 based on Lee and Pottier's method.

shown in Fig. 5.3 (c). The RVI signature was obtained using dual-pol ISAR images, and its randomness value ranged between 0 and 1, as shown in Figs. 5.3 (d) and 5.3 (e). RVI is estimated using a 5×5 boxcar filter via two approaches, one relying only on polarizations and the other on the degree of polarization and eigen-spectrum, respectively. The spatial signatures were qualitatively the same, indicating that the ISAR images can be utilized for RVI estimation. Nevertheless, based on the H-α plane, the scatterings for each case appear in zones 1, 4, and 7, which correspond to high-, medium-, and low-entropy vegetation multiple-scattering zones, respectively, as shown in Fig. 5.4.

5.3 CTF Estimation for CS-ISAR Imaging

Compressive sensing (CS) enables imaging with less data assuming sparsity in certain domains. We proposed a ground breaking coarse-to-fine (CTF) estimation method that reconstructs images with fewer signal supports over fine grids. Owing to the explicit storage and usage within sparse reconstruction, the sensing matrix (SM) is resource-intensive, even for small problem sizes. To alleviate this issue, the CTF procedure discards a certain number of columns from the SM as the reconstruction progresses from coarser to finer scales ($X_{1/F} = 2^{2F}$).

The reconstruction process involves progressively restricting the signal support, thus eliminating a specific number of columns from the SM as the algorithm transitions from one factor to another. The proposed technique does not require a pre-processing chain and introduces a direct reconstruction solution that strategically considers both the computational cost and imaging resolution. The CTF strategy discards the maximum number of unwanted frequencies in the fine stage, reconstructs the image with fewer samples, and achieves a high resolution with negligible clutter. Let $\mathbf{X}$ be a coarseness-scale representation. The scale size $\mathbf{X}_{1/F} \in C^{M\times M}$ increases by a factor of 2^{2F}, where $F \in \{0.25, 0.5, 1\}$ is the coarseness factor (**Coarser, Coarse, Fine**).

Fig. 5.5 shows the scheme for CTF estimation restricted to the feasible signal-support regions. The mask at the coarser level (X4) was obtained by identifying the signal support, which was then transformed into an initial mask for the next coarse level (X2), and only the feasible signal supports were preserved at a fine level (X1). Thus, the fine stage utilizes a few samples from the image vector $\mathbf{S}$ and forces the clutter regions to

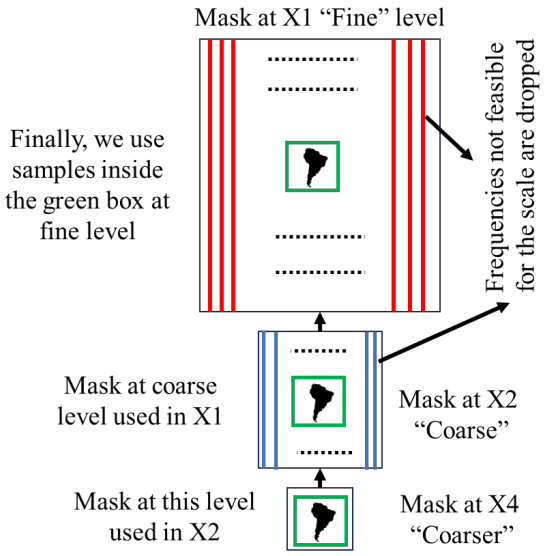

Figure. 5.5 CTF estimation flow graph. Selection of the target mask from the coarser (bottom) to coarse (middle) and fine (top) stages. This allow to remove maximum number of unwanted samples at X1.

have zero values. The image reconstructed at the fine stage attained a resolution higher than the exploited bandwidth as there were frequency gaps.

The imaging results for in-situ data (Yak-42) are presented in Fig. 5.6, utilizing grids of sizes 64×64, 128×128, and 256×256. Fig. 5.6(a) shows the reconstructed images obtained using the 2D FFT method without any motion compensation; however, it requires full cardinality. Fig. 5.6(b) shows images reconstructed via CS-ISAR, employing an SM of discrete Doppler sequences, albeit with high computational demands for the full grid. To address this, we applied the proposed CTF technique, leading to image reconstruction using the LS and OMP methods, as shown in Fig. 5.6(c-d). For the LS approach in the fine stage, as a result of applying the mask, we utilized 4340 (despite 65536) cardinalities from the image vector, whereas the OMP greedy approach employed 2048 cardinalities to achieve high-resolution image reconstruction. We assessed the efficiency of the OMP greedy algorithm in handling image reconstruction at each scale. In conclusion, a multi-scale CTF estimation method is proposed that propagates a mask that restricts the target support across scales, which allows for the restriction of the initial target domain when estimating the ISAR image and the output mask at the next scale. This technique reduces the memory overhead for real-time use in cases where the data samples are limited. This advancement towards low computational costs and lower memory requirements brings us closer to practical applications.

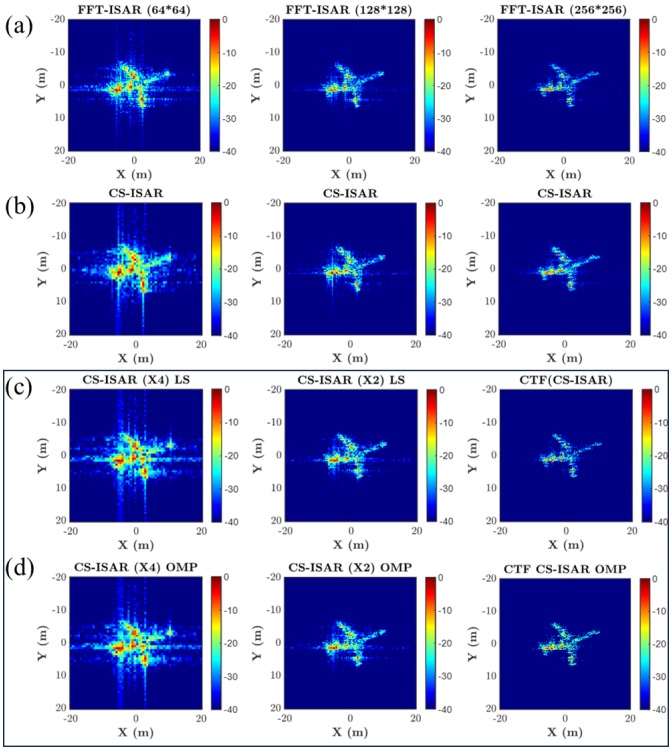

Figure. 5.6 Imaging results for "Yak-42" aircraft. (a) Image focusing using conventional 2D FFT from coarse-to-fine level (b) CS-ISAR imaging using a dictionary of discrete Doppler sequences (c) CTF CS-ISAR imaging using the least squares (LS) method; (d) CTF CS-ISAR imaging using OMP for reconstruction.

Chapter 6

Conclusion

6.1 Conclusion

This thesis thoroughly addresses several aspects of signal processing and spectral analysis of SAR and ISAR data for, imaging, target detection and physical parameter estimation. These include a comparison of three SoA f_{DC} approaches, the proposed stripmap-like processing flow for TOPS SAR, and the extension of the TOPS workflow to incorporate a Deep learning model for preserving Doppler parameters in CV networks. The primary motivation behind developing or modifying these algorithms was to achieve feature and image retrieval with minimal computational costs. One significant advancement is made in Doppler estimation through parallel computing, which not only addresses memory constraints but also proves beneficial for practical and on-board applications. In the realm of ISAR imaging, computation can be expensive due to integrals. To tackle this, imaging through 2D interpolation is proven helpful. This approach proved especially useful for larger grids or target scene imaging, as it greatly reduced the computational cost. This breakthrough opens up possibilities for adapting the technology at security checkpoints for concealed object detection. Lastly, a coarse-to-fine estimation is proposed for Sparse Aperture High-Resolution Imaging. This approach efficiently considers both memory limitations and imaging resolution, leading to significant advancements in this field.

6.2 Future Work

Future lines of research consist of optimizing the solutions developed for the SAR and ISAR setups. With regard to the SAR, possible future work in this area is the testing of the proposed technique with datasets from two different SAR sensors to incorporate along-track interferometry (ATI) for OSC estimation directly observed by the movement of two sensors. Moreover, coastline delineation will be performed by exploiting the data from the two or three SAR sensors to further enhance the applicability of the proposed f_{DC} algorithm to work with all types of SAR data.

Analytical techniques aid in feature extraction and target detection using SAR and ISAR; however, feature classification is equally important. Therefore, deep learning networks are advancing to enhance feature classification from SAR or ISAR data, which will be a privilege to adapt these networks for feature classification accuracy. Building upon the research presented in the context of ISAR, a potential subsequent phase will involve conducting measurements using a bistatic configuration for ISAR. This setup offers a beneficial approach for investigating characteristics of the target, as it enables the acquisition of supplementary data regarding its elevation. The attainment of such topographical insights would demand the development and integration of novel algorithms tailored for bistatic imaging.

6.3 List of original publications

[JP1] M. A. Iqbal, A. Anghel and M. Datcu, "*Coastline Extraction From SAR Data Using Doppler Centroid Images*," in IEEE Geoscience and Remote Sensing Letters, vol. 19, pp. 1-5, 2022, Art no. 1506205, doi: 10.1109/LGRS.2022.3214496.

[JP2] M. A. Iqbal, A. Anghel and M. Datcu, "*Subaperture Decomposition for Ship Detection and Velocity Estimation from SLC SAR data*," IEEE Geoscience and Remote Sensing Letters, (Submitted)

[CP1] M. A. Iqbal, A. Anghel and M. Datcu, "*Doppler Centroid Estimation for Ocean Surface Current Retrieval from Sentinel-1 SAR Data*," 2021 18th European Radar Conference (EuRAD), London, United Kingdom, 2022, pp. 429-432, doi: 10.23919/EuRAD50154.2022.9784550.

[CP2] M. A. Iqbal, A. Anghel and M. Datcu, "*On the De-Ramping of SLC-IW Tops SAR Data and Ocean Circulation Parameters Estimation*," IGARSS 2022 - 2022 IEEE International Geoscience and Remote Sensing Symposium, Kuala Lumpur, Malaysia, 2022, pp. 6817-6820, doi: 10.1109/IGARSS46834.2022.9884331.

[CP3] M. A. Iqbal, R. M. Asiyabi, O. Ghozatlou, A. Anghel, M. Datcu, "*Towards Complex-Valued Deep Architectures with Data Model Preservation for Sea Surface Current Estimation from SAR Data*," In IEEE 20th International Conference on Content-based Multimedia Indexing CBMI-2023, DOI: 10.1145/3617233.3617271.

[CP4] M. A. Iqbal, A. Anghel and M. Datcu, "*Ice Cover Delineation Over Devon Iceland Using Sentinel Polarimetric SAR and Optical Data*", In IEEE International Workshop on Metrology for the Sea; Learning to Measure Sea Health Parameters (MetroSea), 2023, Valletta, Malta pp. 415-420.

[CP5] M. A. Iqbal, A. Anghel, M. Datcu, I. Ederra, and J. C. Iriarte, "*Assessment of mm-Wave High Resolution Inverse SAR Imaging both with Compact and Sparse Data*," 2023 20th European Radar Conference (EuRAD), Berlin, Germany, 2023, pp. 266-269

[CP6] M. A. Iqbal, A. Anghel, M. Datcu, A. Bathelt., S. Sigger, "*Exploiting Inverse SAR Images and Dual-Pol Decomposition For The Estimation Of Tree Scattering Properties*," IGARSS 2023 - 2023 IEEE International Geoscience and Remote Sensing Symposium, Pasadena, USA, 2023, pages 1622 - 1625.

[CP7] M. A. Iqbal, M. H. Conde, A. Anghel and M. Datcu, "*Sparse Reconstruction for High-Resolution Inverse SAR Imaging*", Doctoral Symposium on Electronics, Telecommunications, and Information Technology, 2023, Bucharest, Romania.

[CP8] M. A. Iqbal, M. H. Conde, A. Anghel and M. Datcu, "*Coarse-to-fine Estimation: Compressive Sensing for High-Resolution Inverse SAR Imaging*", In IEEE European Synthetic Aperture Radar Conference (EuSAR), 2024, Munich, Germany, (Submitted)

References

[1] Gang Xu, Bangjie Zhang, Hanwen Yu, Jianlai Chen, Mengdao Xing, and Wei Hong. Sparse synthetic aperture radar imaging from compressed sensing and machine learning: Theories, applications, and trends. *IEEE Geoscience and Remote Sensing Magazine*, 10(4):32–69, 2022.

[2] Alberto Moreira, Pau Prats-Iraola, Marwan Younis, Gerhard Krieger, Irena Hajnsek, and Konstantinos P Papathanassiou. A tutorial on synthetic aperture radar. *IEEE Geoscience and remote sensing magazine*, 1(1):6–43, 2013.

[3] Lei Zhang, Zhi-jun Qiao, Mengdao Xing, Yachao Li, and Zheng Bao. High-resolution isar imaging with sparse stepped-frequency waveforms. *IEEE Transactions on Geoscience and Remote Sensing*, 49(11):4630–4651, 2011.

[4] Muhammad Amjad Iqbal, Andrei Anghel, and Mihai Datcu. Doppler centroid estimation for ocean surface current retrieval from sentinel-1 sar data. In *2021 18th European Radar Conference (EuRAD)*, pages 429–432. IEEE, 2022.

[5] Muhammad Amjad Iqbal, Andrei Anghel, and Mihai Datcu. On the de-ramping of slc-iw tops sar data and ocean circulation parameters estimation. In *IGARSS 2022-2022 IEEE International Geoscience and Remote Sensing Symposium*, pages 6817–6820. IEEE, 2022.

[6] Muhammad Amjad Iqbal, Andrei Anghel, and Mihai Datcu. Coastline extraction from sar data using doppler centroid images. *IEEE Geoscience and Remote Sensing Letters*, 19:1–5, 2022.

[7] Xiufang Zou and Qunying Zhang. Estimation of doppler centroid frequency in spaceborne scansar. *Journal of Electronics (China)*, 25:822–826, 2008.

[8] S Norvang Madsen. Estimating the doppler centroid of sar data. *IEEE Transactions on aerospace and electronic systems*, 25(2):134–140, 1989.

[9] Bertrand Chapron, Fabrice Collard, and Fabrice Ardhuin. Direct measurements of ocean surface velocity from space: Interpretation and validation. *Journal of Geophysical Research: Oceans*, 110(C7), 2005.

[10] Jose Agustin Barrachina, Chenfang Ren, Christele Morisseau, Gilles Vieillard, and J-P Ovarlez. Complex-valued vs. real-valued neural networks for classification perspectives: An example on non-circular data. In *ICASSP 2021-2021 IEEE International Conference on Acoustics, Speech and Signal Processing (ICASSP)*, pages 2990–2994. IEEE, 2021.

[11] Wilhelm Wirtinger. Zur formalen theorie der funktionen von mehr komplexen veränderlichen. *Mathematische Annalen*, 97(1):357–375, 1927.

[12] Reza Mohammadi Asiyabi, Mihai Datcu, Andrei Anghel, and Holger Nies. Complex-valued end-to-end deep network with coherency preservation for complex-valued sar data reconstruction and classification. *IEEE Transactions on Geoscience and Remote Sensing*, 2023.

[13] Emanuele Ferrentino, Andrea Buono, Ferdinando Nunziata, Armando Marino, and Maurizio Migliaccio. On the use of multipolarization satellite sar data for coastline extraction in harsh coastal environments: The case of solway firth. *IEEE Journal of Selected Topics in Applied Earth Observations and Remote Sensing*, 14:249–257, 2020.

[14] Ramona Pelich, Marco Chini, Renaud Hostache, Patrick Matgen, and Carlos López-Martínez. Coastline detection based on sentinel-1 time series for ship-and flood-monitoring applications. *IEEE Geoscience and Remote Sensing Letters*, 18(10):1771–1775, 2020.

[15] Nicolae-Cătălin Ristea, Andrei Anghel, Mihai Datcu, and Bertrand Chapron. Guided unsupervised learning by subaperture decomposition for ocean sar image retrieval. *IEEE Transactions on Geoscience and Remote Sensing*, 2023.

[16] Mozhgan Zahriban Hesari, Ferdinando Nunziata, Giuseppe Aulicino, Andrea Buono, and Maurizio Migliaccio. Analysis of fine-scale dynamics of the drygalski ice tongue in antarctica using satellite sar data. *International Journal of Remote Sensing*, 43(7):2581–2598, 2022.

[17] Risto Vehmas and Nadav Neuberger. Inverse synthetic aperture radar imaging: A historical perspective and state-of-the-art survey. *IEEE Access*, 9:113917–113943, 2021.

[18] Xiahan Yang, Yahong R. Zheng, Mohammad Tayeb Ghasr, and Kristen M. Donnell. Microwave imaging from sparse measurements for near-field synthetic aperture radar. *IEEE Transactions on Instrumentation and Measurement*, 66(10):2680–2692, 2017.

[19] Tiantian Yin, Zhun Wei, and Xudong Chen. Wavelet transform subspace-based optimization method for inverse scattering. *IEEE Journal on Multiscale and Multiphysics Computational Techniques*, 3:176–184, 2018.

[20] Reza Shirvany. *Estimation of the degree of polarization in polarimetric SAR imagery: Principles and applications*. PhD thesis, 2012.

[21] Jong-Sen Lee and Eric Pottier. *Polarimetric radar imaging: from basics to applications*. CRC press, 2017.

[22] Yuanhao Cai, Jing Lin, Xiaowan Hu, Haoqian Wang, Xin Yuan, Yulun Zhang, Radu Timofte, and Luc Van Gool. Coarse-to-fine sparse transformer for hyperspectral image reconstruction. In *European Conference on Computer Vision*, pages 686–704. Springer, 2022.

[23] Jiyuan Chen, Letao Xu, Xiaoyi Pan, Pu Zheng, and Shunping Xiao. High-resolution isar imaging with sparse aperture vfm waveforms under low snr condition. *IEEE Access*, 7:110651–110659, 2019.